NUMERICAL SIMULATION OF SHOCK-STALL FLUTTER OF A HIGH-ASPECT-RATIO FORWARD-SWEPT WING

Koji Isogai
Japan Aerospace Exploration Agency
koji.isogai@nifty.com

Abstract

In order to understand the unusual flutter phenomenon observed in experimental transonic flow for a high-aspect-ratio forward-swept wing, numerical simulations have been conducted using a 3D Navier-Stokes code. The simulations have confirmed that the flutter is a single-degree-of-freedom flutter of the first bending mode in which shock-induced flow separation plays a dominant role. The simulations have also clarified the detailed effects of Mach number and dynamic pressure (particularly the mass ratio) on this type of flutter.

1 Introduction

Divergence is a destructive aeroelastic phenomenon that typically occurs in forward-swept wings. This has long ruled out the practical use of forward-swept wings despite several aerodynamic advantages over conventional aft-swept wings. However, aeroelastic tailoring technology that utilizes the directional stiffness properties of fibrous composites has been changing this situation [1].

Isogai [2] conducted an experimental study on the transonic flutter/divergence characteristics of aeroelastically tailored and non-tailored high-aspect-ratio forward-swept wings. Figure 1 shows the planform and structure of the 1/45-scale aeroelastic wind tunnel model [2] for the wing of a hypothetical 150-seat transport. In this experiment, it was shown that the divergence phenomenon can be successfully suppressed by aeroelastic tailoring. In addition, it was also found that the non-
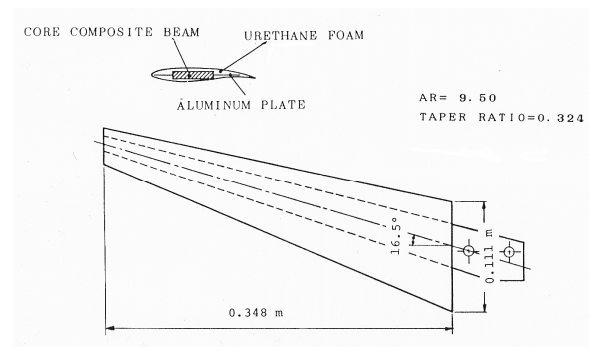

Fig. 1. Planform and Structure of the Wind Tunnel Model [2].

tailored model experienced flutter instead of the divergence predicted by the potential aerodynamic theory (Doublet Lattice Method [3]).

As shown in Fig. 2, the flutter phenomenon experienced by the non-tailored model has the following three unusual characteristics as compared with conventional bending-torsion flutter (classical flutter): 1) the flutter frequencies (64-75 Hz depending on Mach number) are slightly less than the first natural frequency (80.7 Hz) of this model; 2) the flutter dynamic pressure (40 kPa at $M_\infty = 0.715$) at the root angle of attack $\alpha = 2$ deg is far below that of the theoretical divergence dynamic pressure (66 kPa); 3) the flutter boundary depends strongly on the root angle of attack (i.e., the flutter dynamic pressure decreases about 30-40% by changing the root angle of attack from 0 deg to 2 deg). These characteristics seem to suggest that this flutter might be a single-degree-of-freedom flutter in which shock-induced flow separation plays a dominant role. In order to confirm this conjecture qualitatively,
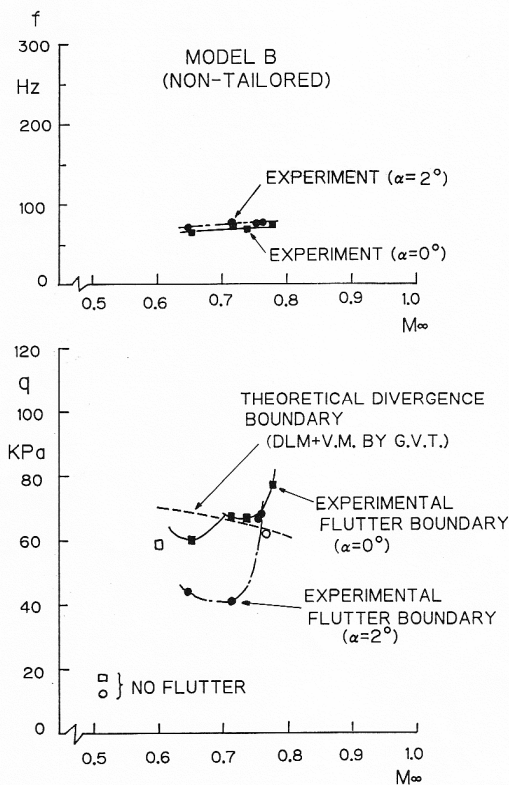
Fig. 2. Transonic Flutter Characteristics of a Non-Tailored Forward-Swept Wing [2].

Yamasaki et al. [4] conducted an experimental study on the transonic flutter of a two-dimensional airfoil that simulates the wash-in mode of a typical section of a non-tailored forward-swept wing. This 2D model is a single-degree-of-freedom system whose axis of pitch is located one chord length downstream from the mid-chord point. Thus, it generates the wash-in mode. In this experiment, they obtained flutter at M_∞ = 0.65, 0.68, and 0.72. The high-speed Schlieren video taken during the flutter clearly showed the existence of shock-induced flow separation, confirming qualitatively that the flutter observed for the non-tailored high-aspect-ratio forward-swept wing is a single-degree-of-freedom flutter in which shock-induced flow separation plays a dominant role; we call this shock-stall flutter. Since shock-stall flutter is an extremely complex phenomenon of fluid-structure interaction induced by the unsteady shockwave and boundary layer interactions, it is a challenge to predict theoretically. The purpose of the present study is to examine the capability of a 3D Navier-Stokes code to predict the shock-stall flutter observed in the non-tailored forward-swept wing reported in Ref. [2] and to clarify the detailed characteristics of this unusual flutter phenomenon.

2 The Wind Tunnel Model and Its Natural Vibration Characteristics

The planform and structure of the wind tunnel model used for the flutter test in Ref. [2] is shown in Fig. 1. It is a straight tapered wing with an aspect ratio of 9.5, a taper ratio of 0.324, a forward sweep angle of the quarter-chord line of 15 deg, a semi-span length of 0.348 m, and a root chord length of 0.111 m. The wing is composed of a core composite beam and urethane foam to provide the aerodynamic contours. The airfoil sections are natural-laminar-flow-type supercritical airfoil sections of an approximately 12% thickness ratio. The core composite beam is located between the 20% and 60% chord lines (see Ref. [2] for

Table 1. Natural Vibration Characteristics of the Wind Tunnel Model.

	f_1 (1B) (f_1/f_1)	f_2 (2B) (f_2/f_1)	f_3 (1T) (f_3/f_1)	f_4 (3B) (f_4/f_1)
G.V.T.	80.7 (1)	304.0 (3.76)	549.0 (6.80)	657.0 (8.14)
B. T.	80.7 (1)	277.7 (3.44)	578.4 (7.17)	640.7 (7.94)
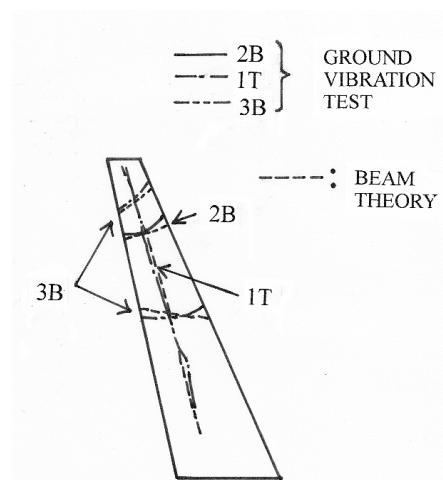
Fig. 3. Comparison of Node Lines Between Ground Vibration Test and Beam Theory [2].

further details of the model). The natural vibration frequencies and the node lines of the non-tailored model, as measured by the ground vibration test, are shown in Table 1 and Fig. 3, respectively. The theoretical values of the natural frequencies and node lines, as calculated by beam theory, are also shown in the same table and figure for comparison. As seen in the table and figure, the theoretical and experimental distributions of the natural frequencies (f_n/f_1) and the node lines are in good agreement. In Fig. 4, the first three natural vibration mode shapes computed using beam theory are shown.

$f_1 = 80.7$ Hz
1st bending

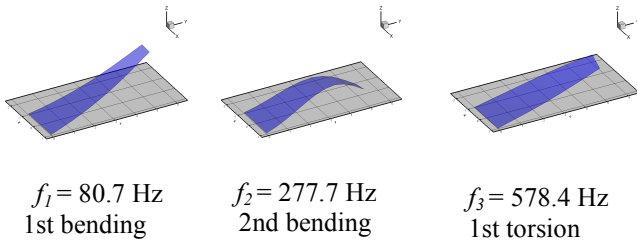$f_2 = 277.7$ Hz
2nd bending

$f_3 = 578.4$ Hz
1st torsion

Fig. 4. Natural Vibration Modes.

3 Numerical Method

As described in Section 1, shock-induced flow separation plays a dominant role in shock-stall flutter. Therefore, it is essential to use a 3D Navier-Stokes code for the prediction of this phenomenon. The 3D Navier-Stokes code used in the present study is a Reynolds Averaged Navier-Stokes (RANS) code originally developed by Isogai [5, 6]. A body-fitted C-H type grid is used, which includes 240 grid points (200 points on the wing and 20 points on the upper and lower surfaces of the wake region) in the chord-wise direction, 29 points in the span-wise direction (19 points on the wing and 10 points on the off-wing region), and 51 points normal to the wing surface. The code uses a total variation diminishing (TVD) scheme [7] and the Baldwin-Lomax algebraic turbulence model [8].

In order to compute the aeroelastic response of the wing, we use the modal approach with the nine natural mode shapes computed from beam theory. The displacement of the wing normal to the wing surface is expressed as

$$f(x,y,t) = \sum_{i=1}^{9} \phi_i(x,y)q_i(t) \qquad (1)$$

where t is time, ϕ_i is the natural vibration mode of the wing, and q_i is the generalized coordinate. Using Lagrange's equations of motion, we obtain the ordinary differential equation of motion for q_i as follows:

$$M_i \ddot{q}_i + \omega_i^2 M_i q_i = \iint_S \Delta p(x,y,t)\phi_i(x,y)dxdy$$

$$\text{for } i = 1,\ldots,9 \qquad (2)$$

where M_i is the generalized mass, ω_i is the natural circular frequency, and Δp is the pressure difference computed using the 3D Navier-Stokes code. Eq. (2) and the 3D Navier-Stokes equations are solved at each time step to obtain the aeroelastic response of the wing. Note that the natural frequencies ω_i used for solving Eq. (2) are corrected up to the 4th mode using the values obtained during the ground vibration test (see Table 1).
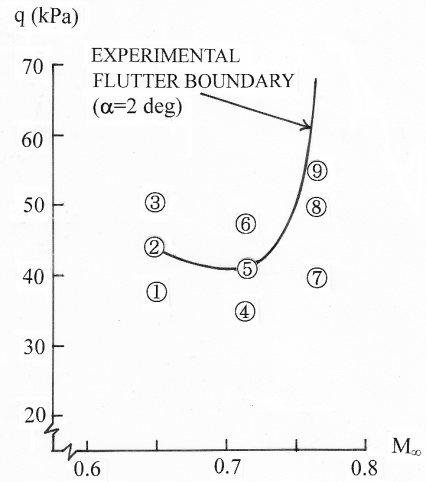
4 Results and Discussion

Fig. 5. Mach Numbers and Dynamic Pressures of the Numerical Simulations.

The present numerical simulations have been conducted around the experimental flutter boundary obtained for the root angle of attack of 2 deg, as shown in Fig. 5. The details for the Mach number M_∞, velocity V, dynamic pressure

q, and mass ratio μ of each case are also given in Table 2. The mass ratio μ is defined by

$$\mu = m / \left\{ \pi \rho_\infty b_0^2 l (\lambda + (1-\lambda)^2 / 3) \right\} \qquad (3)$$

where m is the wing mass, b_0 is the semi-chord length of the wing root, l is the semi-span length, λ is the taper ratio, and ρ_∞ is the free-stream air density. Note that the experimental Reynolds number based on the root chord was 2.3×10^6, while the present numerical simulations were conducted at $R_e = 2.3 \times 10^5$. All of the aeroelastic response calculations reported here were obtained by time-accurate computations that were started impulsively. In the following subsections, the detailed results of the response computations obtained at each Mach number are presented.

Table 2. Flutter Simulations Cases.

Case	M_∞	V (m/s)	ρ_∞ (kg/m³)	q (kPa)	μ
1	0.65	211	1.70	38.0	101
2			1.97	44.0	88
3			2.24	50.0	77
4	0.715	232	1.30	35.0	133
5			1.52	41.0	114
6			1.74	47.0	99
7	0.765	249	1.29	40.0	133
8			1.62	50.0	107
9			1.78	55.0	97

4.1 Results Obtained for $M_\infty = 0.715$ (Cases 4-6)

Figure 6 shows the responses of $\overline{q_i}$ (i = 1, 2, 3) with respect to the non-dimensional time t^* ($t^* = t (V/b_o)$) obtained for Case 5 (q = 41 kPa), which is at the experimental flutter boundary. The term $\overline{q_i}$ is the non-dimensional form of the generalized coordinate q_i defined by $\overline{q_i} = q_i / b_0$. As seen in the figure, the response of $\overline{q_1}$ reaches limit cycle oscillation (LCO) after $t^* = 480$, while the responses of $\overline{q_2}$ and $\overline{q_3}$ are very small compared with that of $\overline{q_1}$. The frequency of $\overline{q_1}$ is 74 Hz, which agrees well with the experimental result shown in Fig. 2. The characteristics of the responses of $\overline{q_i}$ clearly

show that the flutter observed in Fig. 6 is a single-degree-of-freedom flutter of the first bending mode. Figure 7 shows the wing deformation and the flow patterns (iso-density
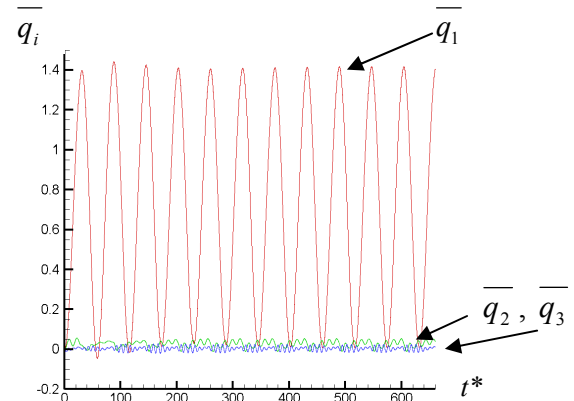

Fig. 6. Responses of the Generalized Coordinates for Case 5 ($M_\infty = 0.715$, q = 41 kPa).

contours around several span-wise sections and the enlarged flow pattern around the 81% semi-span section) during t^* = 472-498 (in the 9th cycle of oscillation). In the figures, we can confirm the appearance, the movement, the disappearance of the shock wave, and the occurrence of shock-induced flow separation during the oscillation cycle. In order to see the correlation between those flow patterns, the aerodynamic force and the displacement of the wing, the responses of the generalized coordinates and the C_L during the 9th cycle of oscillation (t^* = 459-521) are plotted in Fig. 8. The numbers ① to ⑥ shown in Fig. 8 correspond to each flow pattern shown in Fig. 7. As seen in Fig. 8, the lift continues to increase until t^* = 488 (④). Then, it decreases suddenly due to the shock-stall phenomenon at about t^* = 490. This sudden decrease in lift seems to occur due to flow separation at the leading edge, which is observed at the 30-70% semi-span, as seen in the flow patterns at t^* = 493 (⑤). It is clear that the flow separation from the leading edge is induced by the upstream movement of the shock wave accompanied by shock-induced flow separation. It also should be noted that the sudden decrease in lift occurs before the upward deformation of the wing reaches its maximum displacement, as seen in Fig. 8. This enables the

work done by the aerodynamic force to the wing displacement to be positive, and single-degree-of-freedom flutter occurs (a clear explanation of the mechanism of shock-stall flutter can be found in Ref. [4]).
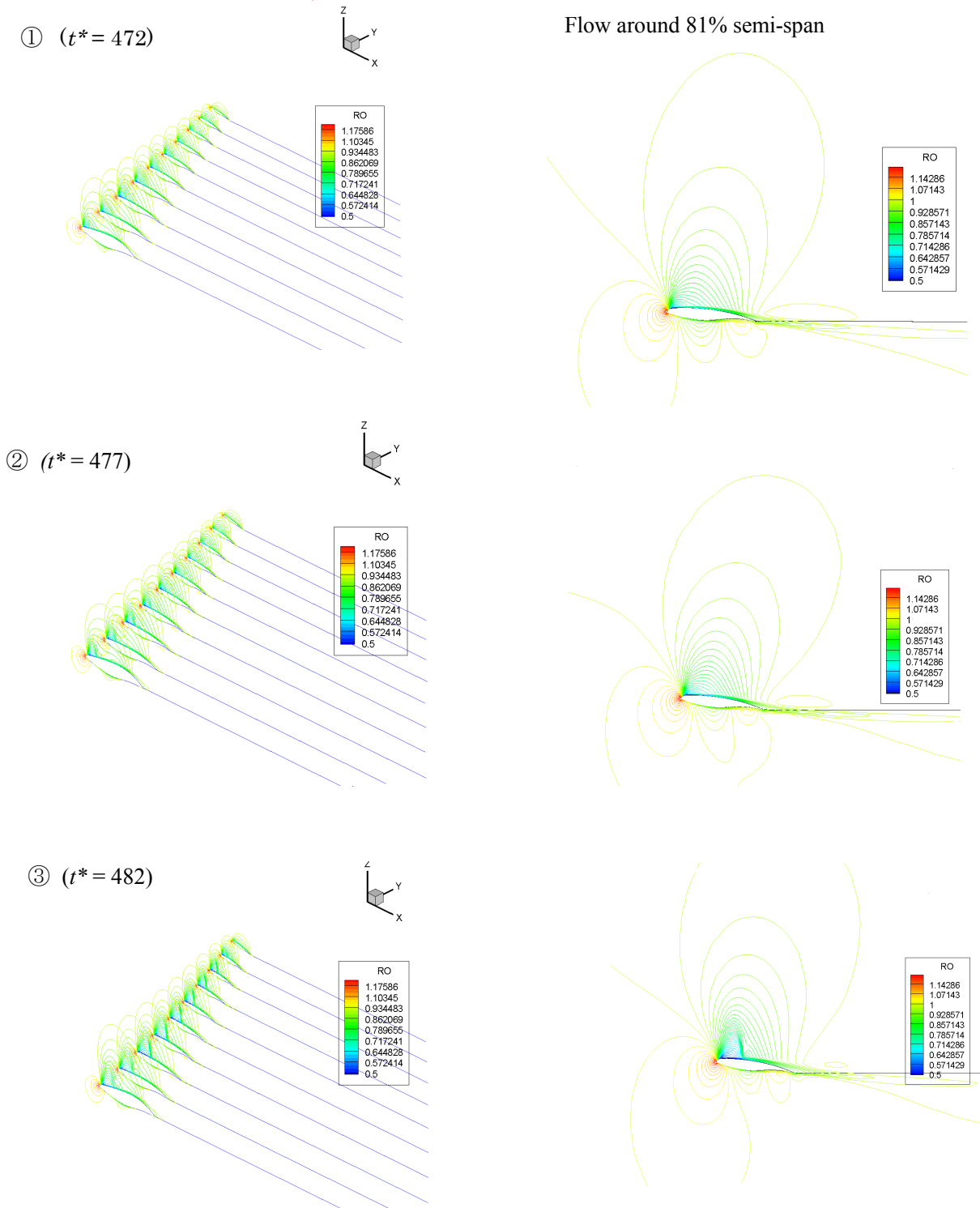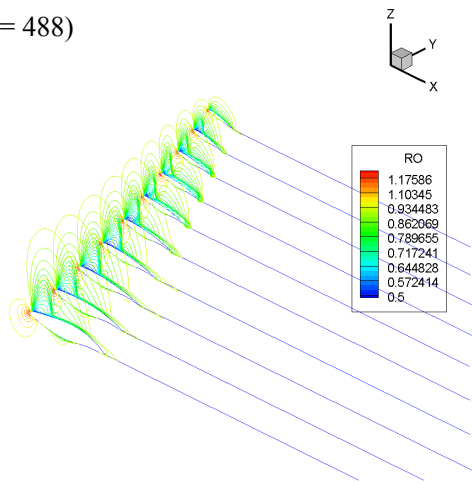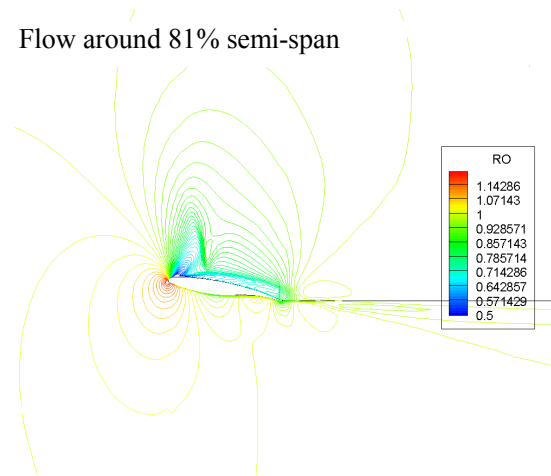
① $(t* = 472)$

Flow around 81% semi-span

② $(t* = 477)$

③ $(t* = 482)$

Fig. 7. Flow Patterns (Iso-Density Contours) during $t* = 472\text{-}498$ in the 9th Oscillation Cycle (Case 5: $M_\infty = 0.715$, $\alpha = 2$ deg, $q = 41$ kPa).
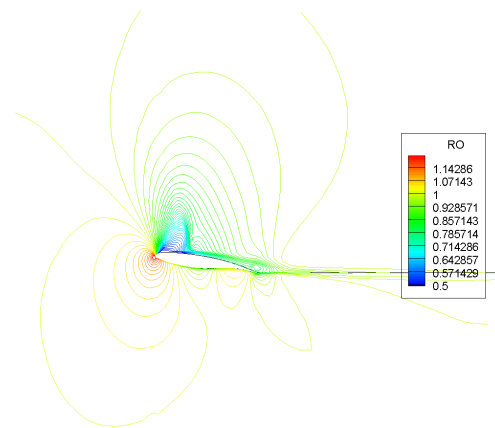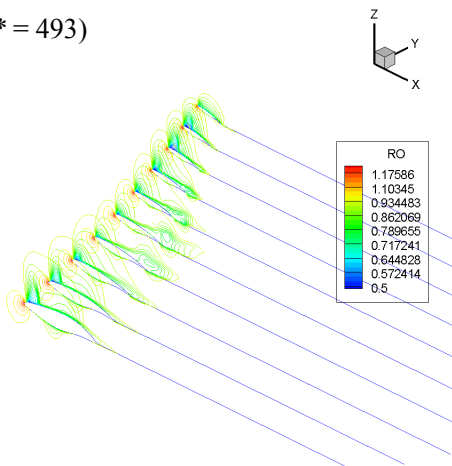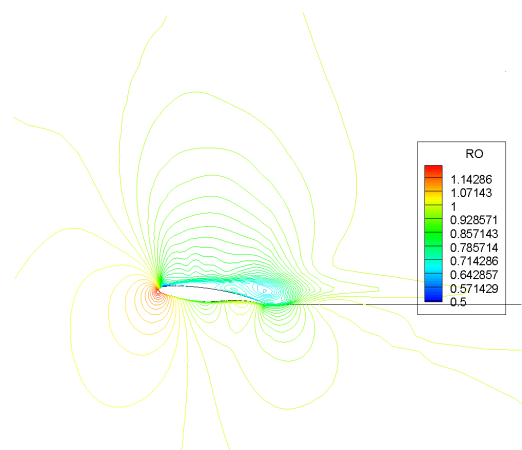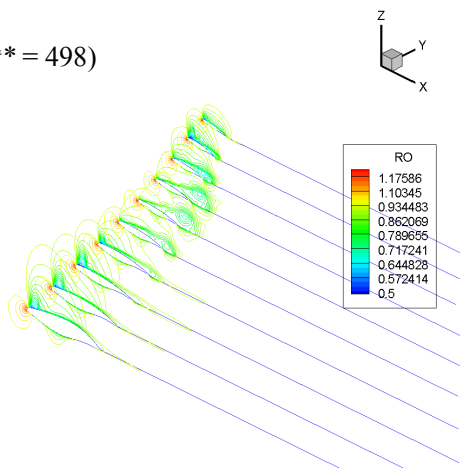
④ ($t^* = 488$)

Flow around 81% semi-span

⑤ ($t^* = 493$)

⑥ ($t^* = 498$)

Fig. 7 (continued). Flow Patterns (Iso-Density Contours) during $t^* = 472$-498 in the 9th Oscillation Cycle (Case 5: $M_\infty = 0.715$, $\alpha = 2$ deg, $q = 41$ kPa).
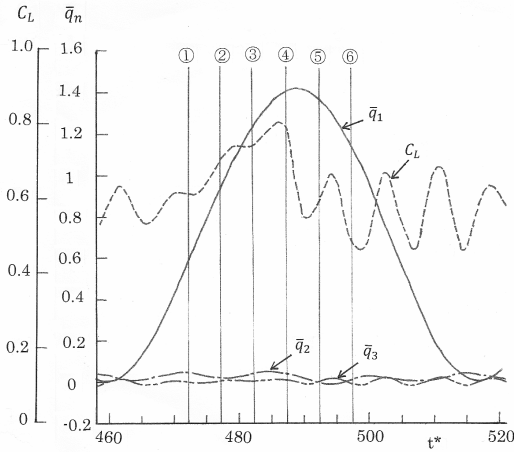
Fig. 8. Variations in Lift and the Generalized Coordinate at the 9th Cycle of Oscillation for Case 5 ($M_\infty = 0.715$, $\alpha = 2$ deg, $q = 41$ kPa).

Fig. 9. Responses of the Generalized Coordinates for Case 6 ($M_\infty = 0.715$, $q = 47$ kPa).

Using the responses of the generalized coordinates, we can easily compute the heaving and pitching displacements with Eq. (1). The time-mean displacements and the amplitudes of the heaving and pitching oscillations of the LCO at the 81% semi-span are $H_{mean} = 0.025$ m, $H_o = 0.025$ m and $\theta_{mean} = 2.5$ deg, $\theta_o = 4.6$ deg, respectively.

Figure 9 shows the responses of the generalized coordinates $\overline{q}_i$ (i = 1, 2, 3) obtained for Case 6 ($q = 47$ kPa). As seen in the figure, we have obtained a slow damping oscillation of $\overline{q}_1$, though the dynamic pressure is larger than in Case 5 ($q = 41$ kPa). However, it seems to be a reasonable phenomenon when we recall that the mechanism of the single-degree-of-freedom flutter is predominant in shock-stall flutter, in which the flutter velocity increases with a decrease in the mass ratio. Note that the mass ratio μ of Case 6 is 99, which is smaller than that of Case 5 ($\mu = 114$).

This reverse tendency of the aeroelastic response of single-degree-of-freedom flutter compared with that of conventional coupled bending-torsion flutter can be confirmed in the response computation for Case 4 ($q = 35$ kPa), where the mass ratio ($\mu = 133$) is larger than in Case 5.
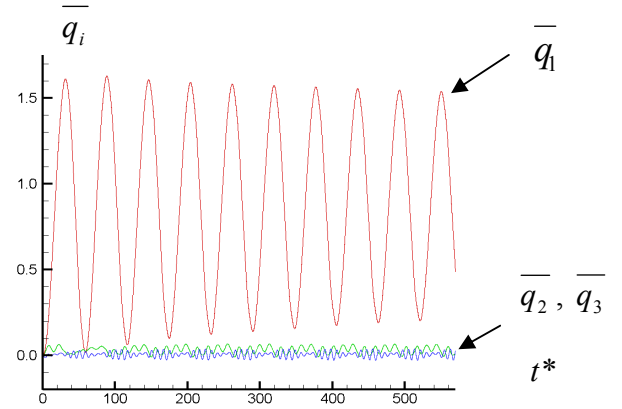
Figure 10 shows the responses of the generalized coordinates $\overline{q}_i$ (i = 1, 2, 3) for Case 4. As seen in Fig. 10, the response of $\overline{q}_1$ reaches LCO after t* = 480. The time-mean displacements and amplitudes of the heaving and pitching oscillations of the LCO at the 81% semi-span are $H_{mean} = 0.021$ m, $H_o = 0.021$ m and $\theta_{mean} = 2.2$ deg, $\theta_o = 3.5$ deg, respectively. Note that the amplitude of the LCO in Case 4 is smaller than in Case 5 because the dynamic
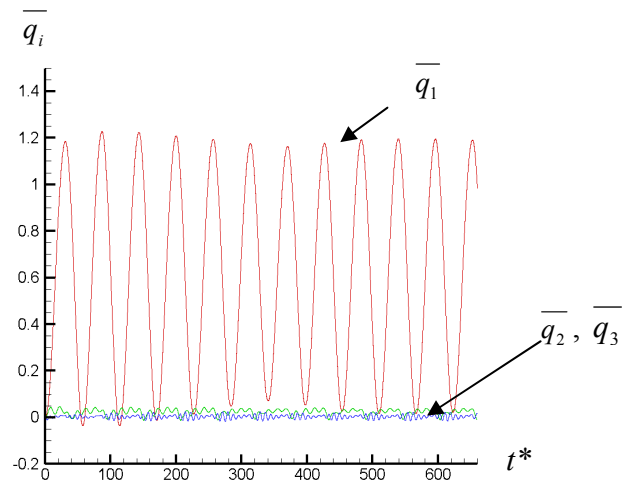

Fig. 10. Responses of the Generalized Coordinates for Case 4 ($M_\infty = 0.715$, $q = 35$ kPa).

pressure in Case 4 is smaller than in Case 5.

4.2 Results Obtained for $M_\infty = 0.65$ (Cases 1-3)

Figure 11 shows the responses of $\overline{q}_i$ (i = 1, 2, 3) with respect to t* obtained for Case 2 ($q = 44$

kPa), which is at the experimental flutter boundary. As seen in the figure, the response of $\overline{q_1}$ reaches LCO, though it has a very low frequency of 9.1 Hz. The predominant frequency of $\overline{q_1}$ is 71.7 Hz, which agrees well with the experimental value shown in Fig. 2. Since the responses of $\overline{q_2}$ and $\overline{q_3}$ are very small compared with that of $\overline{q_1}$, the flutter for this case is a single-degree-of-freedom flutter as well. Figure 12 shows the 3D flow patterns just after the shock-stall phenomenon ($t^* = 928$). The time-mean displacements and the amplitudes of the heaving and pitching oscillations of the LCO at the 81% semi-span are $H_{mean} = 0.028$ m, $H_{o,max} = 0.027$ m, $H_{o,min} = 0.021$ m and $\theta_{mean} = 2.9$ deg, $\theta_{o,max} = 4.4$ deg, $\theta_{o,min} = 3.0$ deg, respectively.
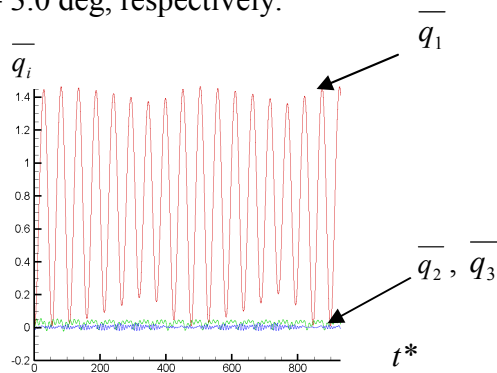

Fig. 11. Responses of the Generalized Coordinates for Case 2 ($M_\infty = 0.65$, $q = 44$ kPa).
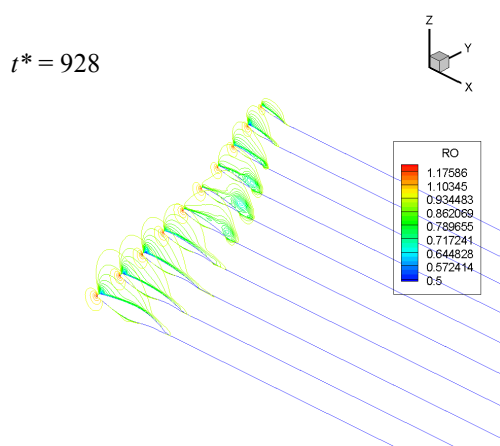

Fig. 12. Flow Pattern for Case 2 Just After the Shock-Stall Phenomenon.

Figure 13 shows the responses of $\overline{q_i}$ (i = 1, 2, 3) with respect to t^* obtained for Case 1 ($q = 38$ kPa). We also obtained a beat-type LCO of $\overline{q_1}$, while the responses of $\overline{q_2}$ and $\overline{q_3}$ are very small compared with that of $\overline{q_1}$. This clearly shows the characteristics of the single-degree-of-freedom flutter; that is, the increase in the mass ratio does not suppress the flutter. Flow patterns similar to those shown in Fig. 12 are also confirmed for this case.
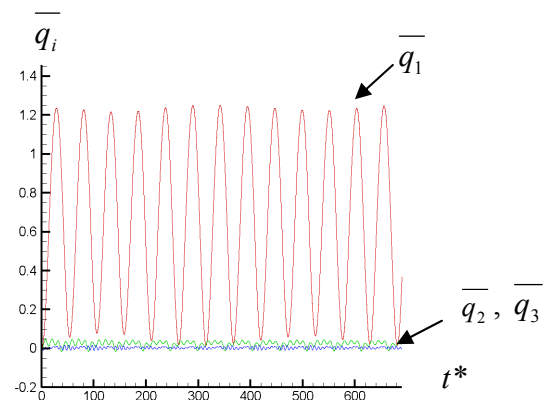

Fig. 13. Responses of the Generalized Coordinates for Case 1 ($M_\infty = 0.65$, $q = 38$ kPa).

Figure 14 shows the responses of $\overline{q_i}$ (i = 1, 2, 3) with respect to t^* obtained for Case 3 ($q = 50$ kPa). As seen in this figure, $\overline{q_1}$ shows strongly damped oscillations, though the dynamic pressure is larger than that of the experimental flutter boundary. However, this phenomenon seems to be reasonable if we recall that this flutter is a single-degree-of-freedom flutter that is suppressed by a decrease in the mass ratio, as already discussed in Section 4.1. Although $\overline{q_1}$ shows a strongly damped oscillation, $\overline{q_2}$ and $\overline{q_3}$ show a high frequency ($f = 488$ Hz) LCO, as seen in Fig. 15, where their responses are shown to become enlarged. Since the frequency of the LCO is close to the natural frequency of the 1st torsion mode ($f_3 = 548$ Hz), it seems to be a single-degree-of-freedom flutter of the first torsion mode. The time-mean displacements and the amplitudes of the heaving and pitching oscillations of the LCO at the 81%

semi-span are H_{mean} = 0.05 m, H_o = 0 m
and θ_{mean} = 4.5 deg, θ_o = 4.9 deg, respectively.
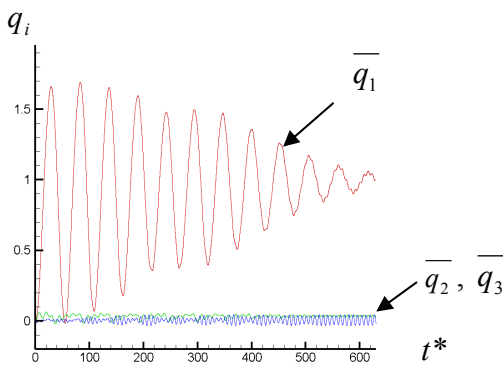

Fig. 14. Responses of the Generalized
Coordinates for Case 3 (M_∞ = 0.65, q
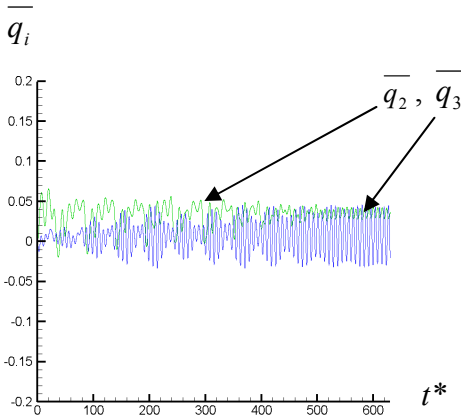= 50 kPa).

Fig. 15. Responses of $\overline{q_2}$ and $\overline{q_3}$ for Case 3
(M_∞ = 0.65, q = 50 kPa).

4.3 Results Obtained for M_∞ = 0.765 (Cases 7-9)

Figure 16 shows the responses of $\overline{q_i}$ (i = 1, 2, 3)
with respect to t^* obtained for Case 8 (q = 50
kPa). As seen in the figure, $\overline{q_1}$ shows a strongly
damped oscillation, while $\overline{q_2}$ and $\overline{q_3}$ show a
high-frequency (f = 532 Hz) LCO, as seen in
Fig. 17, where their responses are shown to
become enlarged. Since the frequency of the
LCO is close to the natural frequency of the 1st
torsion mode (f_3 = 548 Hz), it seems to be a
single-degree-of-freedom flutter of the first
torsion mode. Figure 18 shows the typical flow
pattern observed at t^* = 372. We can confirm
the existence of a strong shock wave and shock-
induced flow separation. Therefore, it is
assumed that the mechanism of the shock-stall

flutter, which is explained in Section 4.1, might
be playing a dominant role for this type of high-
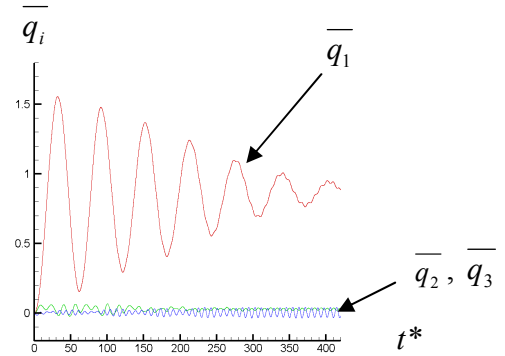frequency LCO as well.

Fig. 16. Responses of the Generalized
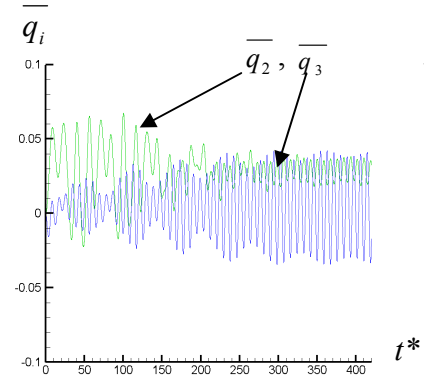Coordinates for Case 8 (M_∞ = 0.765,
q = 50 kPa).

Fig. 17. Responses of $\overline{q_2}$ and $\overline{q_3}$ for
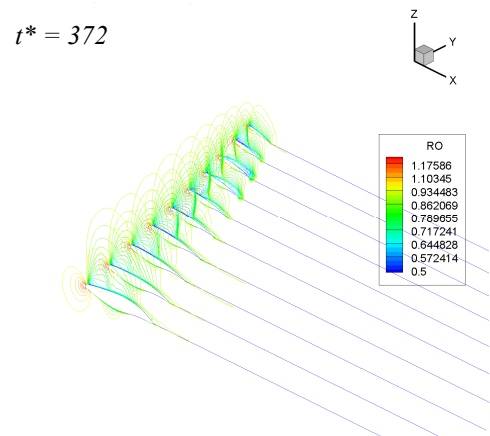Case 8 (M_∞ = 0.765, q = 50 kPa).

Fig. 18. Typical Flow Pattern for Case 8
(M_∞ = 0.765, q = 50 kPa).

The time-mean displacements and the
amplitudes of the heaving and pitching
oscillations of the LCO at the 81% semi-span

are H_{mean} = 0.032 m, H_o = 0 m and θ_{mean} = 3.9 deg, θ_o = 4.6 deg, respectively. Similar responses of the generalized coordinates are also obtained for Case 7 (q = 40 kPa); that is, we have obtained a strongly damped oscillation of $\overline{q_1}$ and a high-frequency LCO of $\overline{q_2}$ and $\overline{q_3}$. The time-mean displacements and the amplitudes of the heaving and pitching oscillations of the LCO at the 81% semi-span are H_{mean} = 0.025 m, H_o = 0 m and θ_{mean} = 3.2 deg, θ_o = 3.2 deg, respectively. As for Case 9 (q = 55 kPa), we have obtained a strongly damped oscillation of $\overline{q_1}$, and no high-frequency LCO of $\overline{q_2}$ or $\overline{q_3}$ such as those observed in Cases 7 and 8 has been obtained.

The results of the response computations are summarized in Fig. 19. As seen in Fig. 19, the correlation between the present numerical simulations and the experimental flutter boundary seems to be good, though the high-frequency LCOs of the first torsion mode, which are predicted by numerical simulation for Cases 3, 7, and 8, were not captured by the experiment since the amplitudes of the heaving oscillation are almost zero for these cases.
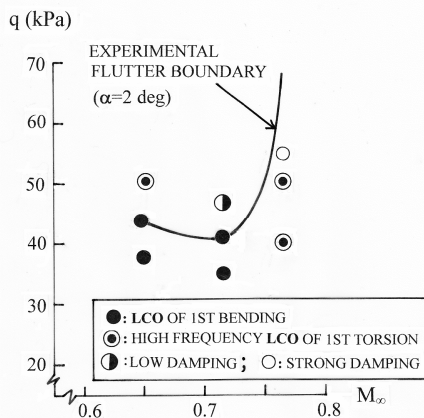

Fig. 19. Results of Numerical Simulations.

5 Concluding Remarks

In order to clarify the unusual flutter phenomenon observed in transonic flow for a non-tailored high-aspect-ratio forward-swept wing, numerical simulations have been conducted using a 3D Navier-Stokes code, and the following results are obtained: 1) The flutter observed in the experiment is a single-degree-of-freedom flutter, in which the first bending mode is exited by the shock-stall phenomenon. 2) The flutters observed in the experiment are LCOs and show the characteristics of a single-degree-of-freedom flutter; that is, the increase in mass ratio does not suppress the flutter. 3) The numerical simulations have predicted the existence of high-frequency LCOs for the first torsion mode in the region where the response of the first bending mode shows strongly damped oscillations.

References

[1] Austin F, Hadcock R, Hutchings D, Sharp D, Tang S and Waters C. Aeroelstic tailoring of advanced composite lifting-surfaces in preliminary design. *Proceedings of the AIAA/ASME/SAE 17th Structures, Structural Dynamics and Materials Conference*, pp. 69-79, 1976.

[2] Isogai K. Transonic flutter/divergence characteristics of aeroelastically tailored and non-tailored high-aspect-ratio forward-swept wings. *Journal of Fluids and Structures,* 6, pp. 527-537, 1992.

[3] Albano E and Rodden W P. Doublet lattice method for calculating lift distributions on oscillating surfaces in subsonic flows. *AIAA Journal,* Vol. 7, No. 2, pp. 279-285, 1969.

[4] Yamasaki M, Isogai K, Uchida T and Yukimura Y. Shock-stall-flutter of a two-dimensional airfoil. *AIAA Journal*, Vol. 42, No. 2, pp. 215-219, 2004.

[5] Isogai K. Numerical simulation of unsteady viscous flow around a flapping wing. *Computational Fluid Dynamics 2002,* edited by Armfield S, et al. Springer, Australia, pp. 701-706, 2002.

[6] Isogai K and Harino Y. Optimum aeroelastic design of a flapping wing. *Journal of Aircraft,* Vol. 44, No. 6, pp. 2040-2048, 2007.

[7] Yee H C and Harten A. Implicit TVD schemes for hyperbolic conservation laws in curvilinear coordinates. *AIAA Journal*, Vol. 25, No. 2, pp. 266-274, 1987.

[8] Baldwin B S and Lomax H. Thin layer approximation and algebraic model for separated turbulent flows. *AIAA Paper* 78-257, 1978.

Copyright Statement